

Analyzing luminescent solar concentrators with front-facing photovoltaic cells using weighted Monte Carlo ray tracing

Shin Woei Leow, Carley Corrado, Melissa Osborn, Michael Isaacson, Glenn Alers, and Sue A. Carter

Citation: [Journal of Applied Physics](#) **113**, 214510 (2013); doi: 10.1063/1.4807413

View online: <http://dx.doi.org/10.1063/1.4807413>

View Table of Contents: <http://scitation.aip.org/content/aip/journal/jap/113/21?ver=pdfcov>

Published by the [AIP Publishing](#)

Articles you may be interested in

[Homeotropic alignment and Förster resonance energy transfer: The way to a brighter luminescent solar concentrator](#)

J. Appl. Phys. **116**, 173103 (2014); 10.1063/1.4900986

[Improved efficiency of organic dye sensitized solar cells through acid treatment](#)

AIP Conf. Proc. **1512**, 774 (2013); 10.1063/1.4791267

[Triple-junction solar cell performance under Fresnel-based concentrators taking into account chromatic aberration and off-axis operation](#)

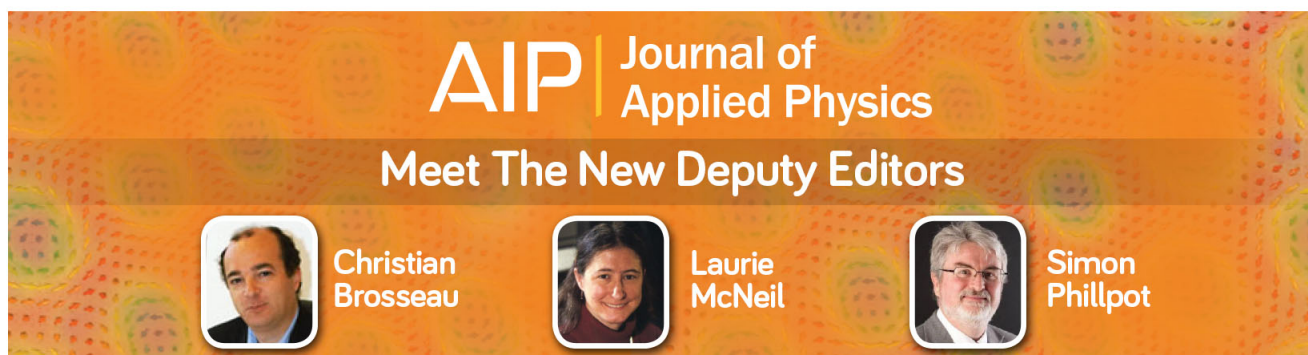
AIP Conf. Proc. **1477**, 81 (2012); 10.1063/1.4753839

[Monte-Carlo simulations of light propagation in luminescent solar concentrators based on semiconductor nanoparticles](#)

J. Appl. Phys. **110**, 033108 (2011); 10.1063/1.3619809

[Tandem dye-sensitized solar cell for improved power conversion efficiencies](#)

Appl. Phys. Lett. **84**, 3397 (2004); 10.1063/1.1723685



AIP | Journal of Applied Physics

Meet The New Deputy Editors

| | | | | | |
|---|---------------------------|---|----------------------|---|-----------------------|
|  | Christian Brosseau |  | Laurie McNeil |  | Simon Phillpot |
|---|---------------------------|---|----------------------|---|-----------------------|

Analyzing luminescent solar concentrators with front-facing photovoltaic cells using weighted Monte Carlo ray tracing

Shin Woei Leow,^{1,2} Carley Corrado,² Melissa Osborn,² Michael Isaacson,¹ Glenn Alers,² and Sue A. Carter²

¹*Jack Baskin School of Engineering, University of California, Santa Cruz, California 95064, USA*

²*Department of Physics, University of California, Santa Cruz, California 95064, USA*

(Received 18 March 2013; accepted 8 May 2013; published online 7 June 2013)

Luminescent solar concentrators (LSC) collect ambient light from a broad range of angles and concentrate the captured light onto photovoltaic (PV) cells. LSCs with front-facing cells collect direct and indirect sunlight ensuring a gain factor greater than one. The flexible placement and percentage coverage of PV cells on the LSC panel allow for layout adjustments to be made in order to balance re-absorption losses and the level of light concentration desired. A weighted Monte Carlo ray tracing program was developed to study the transport of photons and loss mechanisms in the LSC to aid in design optimization. The program imports measured absorption/emission spectra of an organic luminescent dye (LR305), the transmission coefficient, and refractive index of acrylic as parameters that describe the system. Simulations suggest that for LR305, 8–10 cm of luminescent material surrounding the PV cell yields the highest increase in power gain per unit area of LSC added, thereby determining the ideal spacing between PV cells in the panel. For rectangular PV cells, results indicate that for each centimeter of PV cell width, an additional increase of 0.15 mm to the waveguide thickness is required to efficiently transport photon collected by the LSC to the PV cell with minimal loss. © 2013 AIP Publishing LLC.

[<http://dx.doi.org/10.1063/1.4807413>]

I. INTRODUCTION

Building Integrated Photovoltaics (BIPV) is becoming an increasingly attractive method to supplement the high energy needs of today's dense urban cities by generating some of the buildings power requirement on-site. Development in photovoltaic (PV) technology has continuously improved upon the efficiency of PV cells and aggressively reduced their cost, but it still remains expensive relative to competing forms of energy sources. Luminescent Solar Concentrators (LSCs) are static non-imaging concentrators that represent a low cost and simple method to implement BIPV. LSCs achieve higher power outputs per cell area via the concentration of incoming light onto a smaller PV area, and shifting the collected light spectrum to longer wavelengths in which the PV cells exhibit higher external quantum efficiencies.^{1–11} To do this, one or more types of luminescent dyes/particles are infused or coated onto a waveguide. Incident light is absorbed and reemitted at longer wavelengths with a fraction, whose emission angle is larger than the critical angle, remaining trapped in the waveguide through total internal reflection and later redirected to the PV cells. The ability to concentrate both direct and diffuse light negates the need for costly solar tracking systems and allows LSC panels to be incorporated into a variety of locations such as façade claddings in addition to the more commonly found roof top fixtures. With tunable color and partial transparency, the technology can also be applied to windows, skylights, and greenhouse panels.^{12–16} Installation and support structures currently make up half the cost of PV panels on the market. Utilization of BIPV merely adds the cost of the luminescent sheet and PV cells to an existing building structure, saving the cost of the glass substrate and metal frame.

Research on LSCs first started in the late 1970s^{17–20} and has experienced renewed interest in recent years with the advent of luminescent materials with improved ultraviolet stability and quantum efficiency. Available materials include organic dyes, quantum dots (QDs), and semiconducting polymers.^{21–24} Unfortunately, no material possesses all the requisite qualities to make an ideal LSC and each suffer from one or more shortcomings such as a narrow absorption band, self absorption, poor Stoke's shift, low quantum efficiency or rapid degradation. These effects can result in a LSC yielding lower power output than the PV cell used in the LSC if the PV cell was directly exposed to solar irradiation. The low gain can be overcome by mounting the PV cell so that it does not undergo filtering by the luminescent material (a face-mounted structure); however, such structures have not been well studied until recently.²⁵ Such face-mounted structures favor lower concentration factors than edge-mounted structures that can be justified by rapidly decreasing costs of the PV cell itself. Here, we present a detailed Monte Carlo simulation study of face-mounted LSCs.

The power gain (γ_{pwr}) as used in this paper is defined as

$$\gamma_{pwr} = \frac{Power_{panel}}{Power_{ctrl}} = \frac{V_{LSC} \times I_{LSC} + V_{PV} \times I_{PV}}{V_{PV} \times I_{PV}}, \quad (1)$$

where V is the open circuit voltage (V_{oc}) and I the short circuit current (I_{sc}). Subscripts panel and ctrl refer to the LSC panel and reference PV cell, respectively. The gain measures the increase in output power attributed to the addition of a luminescent layer to the panel. The control consists of PV cells with equivalent PV area and position attached to clear

waveguides. In this definition, the fill factors for all PV cells used in experiments are presumed to be equal which agrees with our actual measurements.

LSCs are frequently configured with the PV cell mounted onto the side of the waveguide.²⁻⁸ While high concentration factors are realized, the optical efficiency²⁶ of the panel is often compromised by reabsorption losses and the luminescent particle's limited absorption of the solar spectrum.²⁷ In this work, PV cells are mounted front facing and surrounded by luminescent material to capture both direct sunlight and wave-guided concentrated light, as shown in Fig. 1.²⁵ Such a layout inherently guarantees that γ_{pwr} per cell is greater than one and imparts flexibility with cell positioning and area coverage when attempting to balance the level of light concentration against losses from re-absorption. The LSC panel is further separated into a thin luminescent absorbing layer on the back of a thick waveguide, thereby extending the mean-free-path (MFP) between absorption events.²⁶ Efficiency of the system is given by

$$\eta_{panel} = \left(\frac{A_{PV}}{A_{panel}} \right) \eta_{PE} + \left(\frac{A_{LSC}}{A_{panel}} \right) \eta_{PL} \times \eta_{abs} \times \eta_{WG} \times \eta_{DC} \times \eta_{MPE}, \quad (2)$$

where A is the area and η is the efficiency. The subscripts panel, PV, PE, PL, abs, WG, DC, and MPE refer to the overall panel, PV cell, PV conversion efficiency, dye photoluminescence, dye absorption, waveguide, wavelength down-conversion and efficiency at emission wavelength, respectively.

Although PV cells have comparatively high efficiency per unit area, they typically cost an order of magnitude more than the acrylic waveguide and luminescent dyes used in the LSC. The goal of this work is not to maximize the LSC panel's power conversion efficiency as that can always be achieved by increasing the fraction of PV cells to achieve a power efficiency of up to 20%. Instead our focus is to reduce the cost per watt of power generation while enabling the

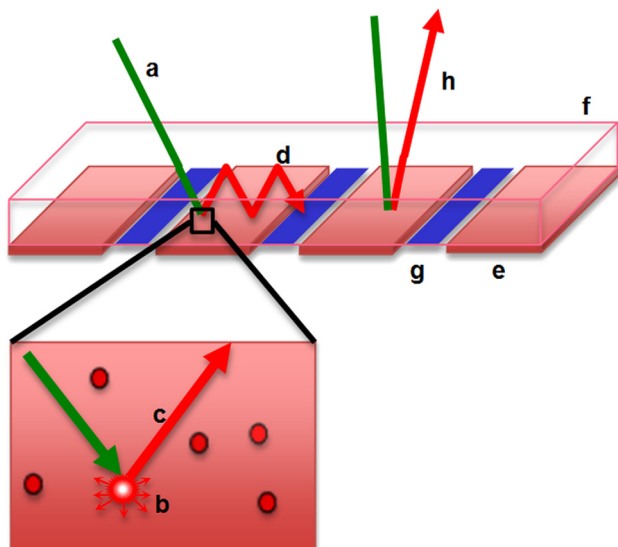


FIG. 1. Schematic of the LSC panel. (a) Incident photon; (b) luminescent particle; (c) re-emitted photon; (d) wave-guided photon; (e) luminescent layer; (f) waveguide; (g) PV cell; (h) photon escape-cone trajectory.

transparency needed for window integration. For simulations and later experiments, a commercial dye (LR305) and silicon PV cells were used, fixing the values of η_{PE} , η_{DC} and η_{MPE} . This leaves the LSC to PV cell area ratio and remaining efficiency variables as design parameters to be determined. Dye concentration alters the absorption (η_{abs}) and photoluminescence efficiency (η_{PL}), with higher concentrations not only improving absorption but also leading to PL quenching due to dye aggregation. Reabsorption loss is also adversely affected by high concentration when significant overlap exists between the absorption and the emission spectra of the dye. Waveguide efficiency (η_{WG}) comprised many factors including waveguide surface conditions, embedded scattering centres, its refractive index, and owing to the forward facing PV cell design, matching between the waveguide thickness and the PV cell dimension. The LSC to PV ratio will be determined by a trade off between the power conversion efficiency, cost per watt desired, concentration factor, and reabsorption losses. This paper builds upon the results in Ref. 25 by providing Monte Carlo simulations that trace each photon and therefore allow determination of the mechanisms behind how photons are lost or efficiently converted to power. This provides insight into the operation of the LSC as well as how to improve its efficiency through modification of the design.

Optimizing the system experimentally is time consuming, costly and often does not provide an adequate understanding of the physical parameters involved. A ray tracing simulation based on the Monte Carlo method^{3,26,28-33} has been developed, incorporating the measured absorption/emission spectra of the luminescent dye dispersed in thin acrylic, and the background scattering effects of acrylic. Simulation results closely parallel data collected from constructed mock up panels and permit detailed study of the distribution of photons and various loss mechanisms present in the LSC panel. The non-linear change in γ_{pwr} with LSC:PV-cell area implies the existence of an optimum ratio and hence the ideal cell to cell separation. For a rectangular PV cell, matching the waveguide thickness and PV cell width produces the highest γ_{pwr} . Simulations reveal how γ_{pwr} is affected by both parameters and the means by which this occurs.

In Sec. II, the workings of the ray tracing program are explained. The analysis of several LSC panel simulations, comparisons with experimental data, and the implications on the panel design follow in Sec. III. The various loss modes present in the LSC are also examined. Finally, Sec. IV summarizes the work and conclusion.

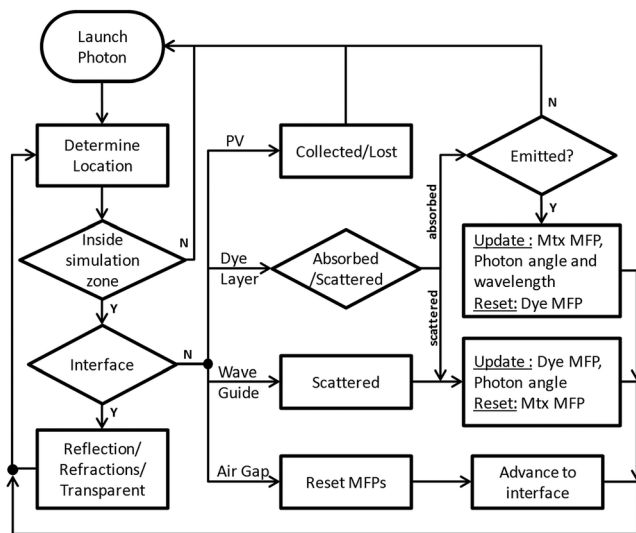
II. WEIGHTED MONTE CARLO RAY TRACING SIMULATION

Ray-tracing has often been used to model optical systems in many applications, particularly where wave effects can be ignored. Monte Carlo ray-tracing models for LSCs while not as fast as thermodynamic models^{4,34,35} is a less complex and hence easier model to implement. It affords greater flexibility in altering the panel dimensions and multiple physical effects included in the model. The LSC model consists of layered planar structures divided into several

regions as shown in Fig. 1. A single layer of acrylic forms the top of the panel. The second layer is broken into regions of thin acrylic infused with LR305, interspaced by PV cells. Because the PV cells are much thinner than the surrounding luminescent layer, an air gap is added below each PV cell in the model to make up the difference and account for the rare occurrence when photons travel beneath the PV cell. Rectangular boxes are used initially to simplify analysis, but the program is able to handle non-rectangular dimensions and can simulate any number of additional layers.

The ray-tracing program follows the path of each individual photon launched at the LSC panel, tracking its position and interaction within the panel until termination, either via collection by a PV cell or lost through non-radiative absorption and escape trajectories. The path and interactions of a photon are strongly influenced by its wavelength. Solar radiation is non-uniform in its wavelength distribution and is dependent on a number of factors such as geographical location, time of day, season and prevailing weather conditions. A weighted Monte Carlo algorithm^{36–38} is employed to incorporate this biased probability into the determination of photon outcomes. The initial wavelength of illuminating photons is randomly selected but skewed in its distribution to replicate the AM 1.5 solar spectrum over a large number of samples. To adequately reproduce the spectrum and obtain statistically reliable results, a minimum of 10^5 photons were simulated in each run. The photon is given an initial direction, and the starting position on the LSC top surface is randomly determined to distribute photons evenly over the entire panel length or any desired region.

Fig. 2 depicts the ray-tracing simulation algorithm. In summary, based on the photon's current location and simulation parameters, the event (absorption, scattering, interface interaction, collection, loss) that is first encountered along the photon's direction is determined; this gives the path length travelled and hence the new photon location. Event



Mtx MFP = Photon Mean Free Path in Matrix
Dye MFP = Photon Mean Free Path in Dye

FIG. 2. Ray-tracing algorithm flow chart. The simulation is broken up into several distinct mutually exclusive interactions, namely the interface and layer effects on the photon. Determining the photon location applies the appropriate action for each iteration.

specific interactions are evaluated updating the simulation parameters and the photon's current state. In accordance with the Monte Carlo method, outcomes of photon interaction with interface boundaries, luminescent particles, and scattering centers are determined by comparing calculated probabilities with randomly generated numbers. At the PV cell, a photon is deemed to have been successfully collected when it strikes the top of the cell from above and has an energy above the bandgap of the silicon PV cell, namely 1.1 eV. Any other approach or position hit is recorded as a loss. Collected photons are further categorized into those with and without sufficient energy to generate photocurrent. Only current generating photons are counted towards γ_{pwr} calculations.

A. Photon localization

The prevailing effects acting on the photon depend on its locale. Localization is carried out by simultaneously comparing the photon's current coordinates with the boundary of every region in the simulation zone. To cover a multitude of conditions, two localization tests^{39,40} (line intersection and point-in-box) are applied. Each test identifies a set containing one or more regions in which the photon might reside in. Both sets intersect at only one region, which always produces the correct outcome.

1. Line intersection test

The light ray and the interface vectors are each defined by a point plus a direction vector

$$\text{Light Ray : } Q(r) = Q_0 + r\vec{v}, \quad \text{Interface : } P(s) = P_0 + s\vec{u}. \quad (3)$$

By setting \vec{v} and \vec{u} to the mean-free-path and length of the interface, respectively, we can determine a result from the sign and magnitude of r and s . A successful ray-interface intersection occurs when the ray is projected to cross the interface in front of the ray ($r > 0$) and within the length of the interface ($0 \leq s \leq 1$). If intersection occurs at a distance longer than the mean-free-path ($r \geq 1$), then an absorption or scattering event flag is raised.

From the vector diagram (Fig. 3), we have at the point of intersection

$$P(s') - Q_0 = w + s'\vec{u} = r\vec{v}, \quad (4)$$

since $r\vec{v}$ is perpendicular to \vec{v}_\perp : $\vec{v}_\perp \cdot (w + s'\vec{u}) = 0$.

Rearranging to solve for s'

$$s' = \frac{-\vec{v}_\perp \cdot w}{\vec{v}_\perp \cdot \vec{u}} = \frac{v_y w_x - v_x w_y}{v_x u_y - v_y u_x}. \quad (5)$$

Similarly for r , we have $s'\vec{u}$ is perpendicular to \vec{u}_\perp , hence $\vec{u}_\perp \cdot (-w + r'\vec{v}) = 0$

$$r' = \frac{\vec{u}_\perp \cdot w}{\vec{u}_\perp \cdot \vec{v}} = \frac{u_x w_y - u_y w_x}{u_x v_y - u_y v_x}. \quad (6)$$

By projecting the photon's path from its current location and examining the intersections it makes with the boundary of

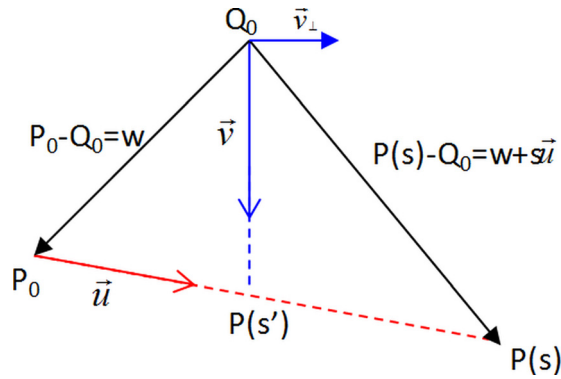


FIG. 3. Vector diagram illustrating the line intersection test. \vec{u} and \vec{v} are the unit vectors of each line. w is a vector joining the points of origin for each line and $P(s)$ the point of intersection.

the region, we can determine if the photon is currently inside or outside the region. In the majority of circumstances, if the defined region is a convex polygon, a light ray originating from within will intersect with only one interface of the region. For a concave polygon, multiple boundary intersections can occur. An odd number of interface intersections indicate that a photon is within the region. One drawback is that this test fails to discriminate the photon's position accurately when the photon is projected to intersect with one or more vertices of the actual region it is residing in.

2. Point-in-box test

This test uses the two-point method to describe a line. Each region in the simulation is delineated by a polygon which can be decomposed into a number of straight lines. Given two consecutive vertices, (x_1, y_1) and (x_2, y_2) , the line equation derived from the slope is given as

$$\frac{y_2 - y_1}{x_2 - x_1} = \frac{y - y_1}{x - x_1} \xrightarrow{\text{rearranging}} (y_2 - y_1)x + (x_1 - x_2)y + y_1x_2 - x_1y_2 = 0. \quad (7)$$

Substituting the coordinates of the photon into the left hand side will yield a number indicating its position relative to the line, with zero being exactly on the line. A positive or negative number signifies that the photon is either on the right or left of the line, with respect to the line direction, depending on the order of the vertices used. Performing the tests in a clockwise direction, a photon is deemed to be within a region when it lies to the right of all lines that make up the region's boundary. A limitation to this test occurs when the photon position is exactly on a boundary, in which all regions adjacent to that boundary would be marked as being positively identified.

B. Interface interaction

In the algorithm, we consider three classes of interface that represents the possible boundary interactions in the LSC panel. The simplest class is a transparent interface, which represents the boundary between adjacent optically coupled regions. The photon is allowed to simply pass through with no additional effects. The next class is that of a reflective

interface, where a photon undergoes a reversal in the direction normal to the reflective plane. This class can be configured to be partially absorbing by comparing the result from a random number generator and the probability of absorption. The last class of interface presents a refractive surface to the photon where the photon is either reflected or refracted. With the assumption of unpolarised light, the reflection coefficient is calculated using Fresnel's equation

$$R = \left[\left(\frac{n_1 \cos \theta_1 - n_2 \cos \theta_2}{n_1 \cos \theta_1 + n_2 \cos \theta_2} \right)^2 + \left(\frac{n_1 \cos \theta_2 - n_2 \cos \theta_1}{n_1 \cos \theta_2 + n_2 \cos \theta_1} \right)^2 \right] \div 2, \quad (8)$$

where the subscripts 1 and 2 represent the incident and transmitted zones, respectively.

Although the refractive index of acrylic varies slightly with wavelength,⁴¹ a fixed index of 1.491 is chosen for simplicity.

C. Absorption, emission, and scattering

The acrylic waveguide has high optical transparency, but for large panels, trapped photons can travel long distances in the waveguide, thus matrix (Mtx) scattering should be considered. The MFP of a photon can be calculated from transmission measurements using the Beer-Lambert law given as

$$MFP = \left| \frac{t}{\ln[T(\lambda)]} \right|, \quad (9)$$

where t is the thickness of sample and $T(\lambda)$ is the transmission level measured for each wavelength.

The Mtx MFP is substituted into the line intersection test described earlier to determine if a boundary collision or scattering event arises first. Scattering is assumed to be perfectly elastic and a new random direction is assigned to the photon. The Mtx MFP is tracked at all times and should other events precede scattering, the distance travelled is subtracted from the current MFP and reused in the next iteration. Whenever the photon leaves the acrylic matrix (e.g., refracts into the air gap), the Mtx MFP is reset to its maximum value as determined by (9).

Luminescent particles in the dye layer act as a second scattering center overlying the acrylic matrix. As the two scattering/absorption events are considered independently, a second mean-free-path is introduced for the dye (Dye MFP) calculated using the absorption spectrum measured (Fig. 4). Spectrometer (N&K UV-vis) readings were taken, with a clear acrylic sheet of the same thickness acting as the baseline; hence, the results obtained are purely attributed to the LR305 dye. The two MFPs are compared at each iteration, with the smaller value substituted into the intersection test. The Dye MFP is tracked and updated similarly to Mtx MFP; whenever the photon leaves the dye layer, Dye MFP is reset. This can be extended to include more than one luminescent particle or scattering centers to model a multi-dye LSC or one infused with nanoparticles.

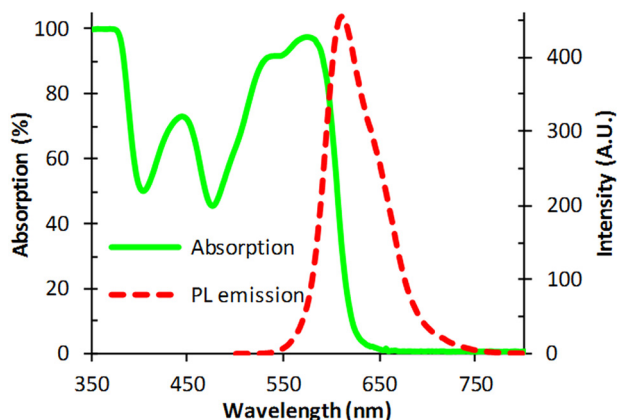


FIG. 4. Absorption (solid) and emission (dotted) spectra of LR305 in acrylic with clear acrylic as the reference baseline.

The measured quantum efficiency of LR305 in acrylic is 85%.²⁵ A random number is compared against this figure to determine if photon re-emission occurs. Emission is assumed to be isotropic and a random angle is assigned. Emission wavelength selection follows the same weighted algorithm as the initial photon and has its distribution weighted to the photoluminescence spectra (Fig. 4) measured (LS-45 Perkin Elmer spectrometer).

III. SIMULATION RESULTS

An array containing the vertex coordinates of all regions in the LSC model is provided as input. The initial photon angle can either be defined or randomly selected. The number of PV cells, their position, and the number of layers can all be varied to model a number of different LSC panel designs. To obtain a qualitative feel on the behavior of photons in the LSC, the photon trajectories can be imaged onto a 2-dimensional panel representation. Fig. 5 shows the visualization of a LSC panel with two PV cells; each event encountered by the photon can be clearly distinguished.

A. Waveguide thickness and cell dimensions

For trapped photons in the waveguide, the horizontal distance traversed in plane is determined by the waveguide thickness and given as

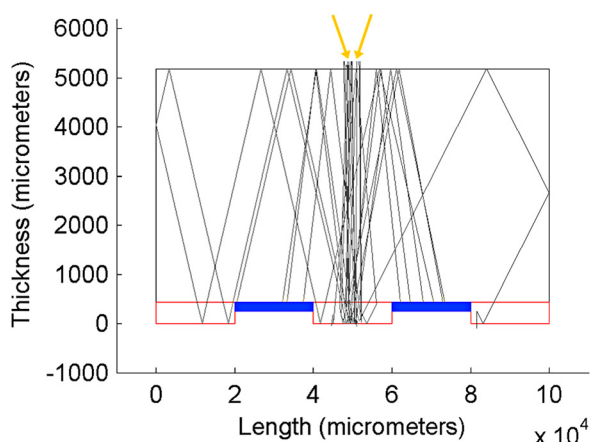


FIG. 5. Visualization of simulated waveguided rays in the LSC panel with an incident spot size of 5 mm and an entry angle of $\pm 40^\circ$.

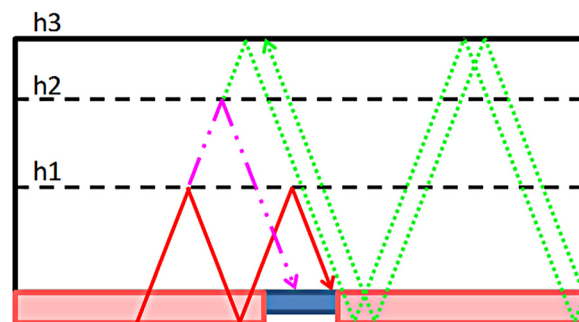


FIG. 6. Illustration of the effect waveguide thickness and PV cell width has on the transport efficiency of photons to the PV cell.

$$\Delta x = h \tan \theta \tag{10}$$

where h is the waveguide thickness and θ is the photon direction with respect to the plane normal. Thicker waveguides help suppress reabsorption by allowing photons a longer travel path in the dye-free waveguide. The design objective for LSCs is to channel photons to the PV cell with minimal reabsorption. For front mounted PV cells, a situation arises in which there exists an ideal waveguide thickness for each PV cell dimension. As illustrated in Fig. 6, waveguides that are too thick or thin increase the number of reflections, and thus interactions a photon endures with the luminescent layer before striking the PV cell.

Standard glass thickness used in windows is between 2-6 mm. In this paper, acrylic with similar optical transmission as glass was used as the waveguide material. Standard PV cells purchased are 12.5 cm by 12.5 cm. From these, 1 cm or 2 cm wide strips were readily diced and used in panel construction. A single cell was placed in the middle of the LSC and simulations for increasing waveguide thickness were executed for each cell width. The number of trapped photons that were collected by the PV cells was recorded and the results are shown in Fig. 7. With LR305 as the luminescent species, peak collection occurred at approximately 2 mm and 3 mm thickness for the 1 cm and 2 cm wide cells, respectively, with the 2 cm wide cells exhibiting greater robustness to waveguide thickness variations. A thicker luminescent absorbing layer will exacerbate reabsorption losses increasing the curve roll-off on either side. For large panel structural

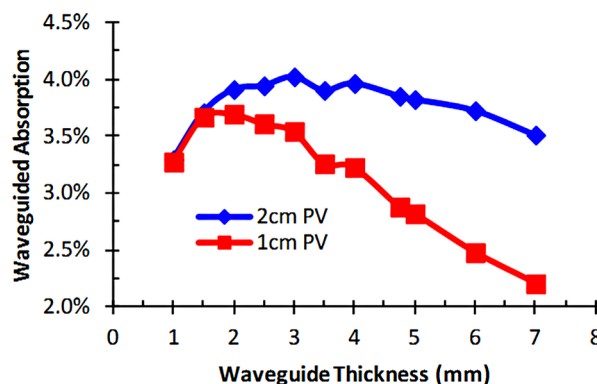


FIG. 7. Photons collected by PV cell through waveguiding action as a percentage of total photons, versus waveguide (acrylic) thickness for a single 1 or 2 cm wide cell.

integrity, a final thickness of 3/16 in. (4.76 mm) was chosen instead.

Since both direct and indirect light are being collected, γ_{pwr} is maximized when waveguided photons are able to reach all parts of the PV cell and are evenly distributed across its surface. To better understand the physical effect, cell widths were varied on a 3/16 in. thick waveguide and simulated. The PV cell length is divided into 500 μm sections. Coordinates of every waveguided photon collected by the PV cell are recorded and each photon is assigned to one section. From Fig. 8, photon concentrations initially become more even as the cell width increases. From 4 cm onwards, a marked decline in photons reaching the middle of the cells is observed, indicating that parts of the cell were not being enhanced by the LSC, resulting in a decrease in γ_{pwr} . On very wide cells, the middle received only direct illumination with virtually all of the photons absorbed within 3 cm from the edge. Together with the waveguide thickness simulations, we can estimate that each centimeter of PV cell width requires an additional 0.15 mm of waveguide thickness for the best result. The eventual thickness of the LSC panel though would be dictated by more practical issues such as cost, weight, strength, and accepted standards in industry.

B. Panel layout

Larger area of LSC increases the quantity of photon captured by the LSC panel which in turn raises the LSC current contribution. As such, from (1), γ_{pwr} is expected to improve with higher LSC to PV cell ratio. In opposition to this, photons captured by the LSC further away from the PV cell

experience higher probabilities of reabsorption and scattering, which may negate any augmentation by the LSC. An optimum LSC to PV ratio results in the highest γ_{pwr} per area LSC added. This in turn would translate into the optimum separation between PV cells on the LSC panel. A series of simulations with increasing panel size were carried out and γ_{pwr} plotted. The PV cell width was set at 2 cm and the illumination angle normal to the LSC panel.

Simulation results in Fig. 9 show an initial linear increase in γ_{pwr} with LSC size which gradually approached a plateau. The linear portion indicates that the additional photons captured by extending the LSC experience little or no reabsorption/scattering events. The simulation suggests that each PV cell should have 7-9 cm of LR305 luminescent material on each side for the highest improvement in γ_{pwr} per area LSC added.

To corroborate this experimentally, a mock up LSC panel was constructed and tested outdoors. To approximate different sized panels, areas of the LSC panel were masked off to block incoming sunlight. Measurements were taken from 1 to 3 pm in the middle of September, which places the sun at approximately 48° from the horizon.⁴² A setup replicating the experiment was simulated; a comparison of the two results in Fig. 10 shows a high degree of correlation with an offset between the two. The non-linear transition occurs more gently but begins at about the same point as before, with the mask edge around 7-9 cm from the PV cell.

The difference between experimental and simulation results can be attributed to an overestimation of the overlap between the LR305 absorption/emission curves which leads to higher reabsorption losses in the simulation model.

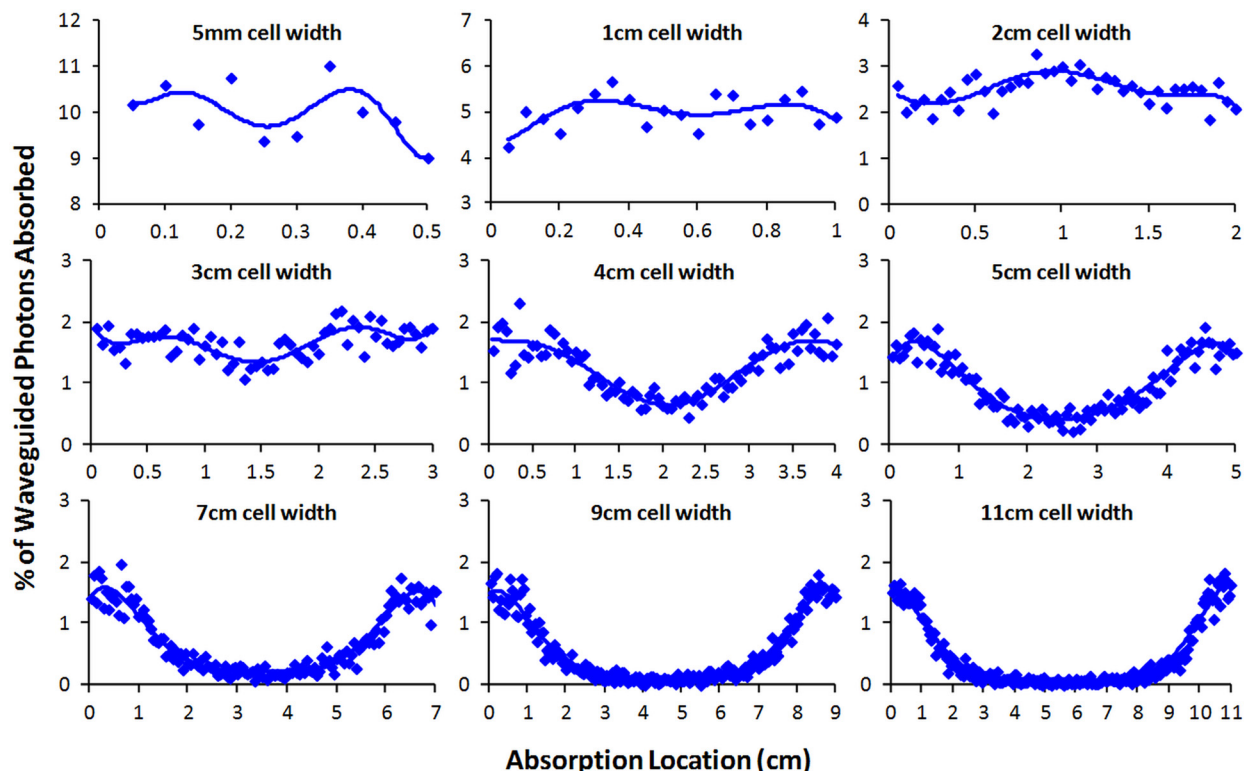


FIG. 8. Waveguided photons absorbed by the PV cell are counted and grouped by the position absorbed. PV cell length is divided into 500 μm sections each representing a group. Waveguide thickness: 4.76 mm (follows experimental panels).

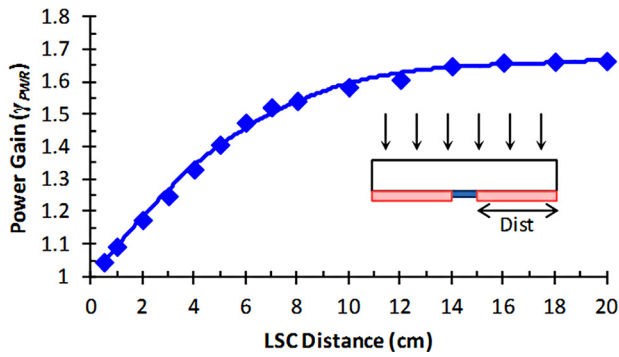


FIG. 9. Power gain versus increasing LSC panel length on each side of the cell. PV cell width: 2 cm, photons incident angle: 0° with respect to plane normal.

Differences in the reference used for γ_{pwr} calculation are also a contributing factor. Experimental results make use of a completely masked of cell (0 cm LSC on each side) as a base line. Whereas in simulation, the number of photons from direct illumination collected by the PV cell in each run is used as the base line.

C. System response to illumination angle and edge surface treatment

An advantage often cited for LSCs is the ability to collect indirect or diffuse light, enabling it to eliminate the need for solar trackers found in other concentrator systems. To study the operating range of the LSC panel as the sun angle changes, the composition of photons collected by the PV cell was extracted from simulations and plotted (Fig. 11). The setup consists of a 2 cm wide PV cell with 10 cm of LR305 luminescent material on each side and reflective panel edges. Light intensity on the LSC surface was diminished accordingly with the cosine of the solar zenith angle. Fig. 11(a) is plotted as a percentage of the total incoming photons on the panel surface. Fig. 11(b) shows the same graph but with percentages referenced to the maximum solar intensity when the solar zenith angle is at 0°.

Over a large range of angles, photon contribution from the LSC remains fairly constant with a slight increase at higher solar zenith angles. Direct illumination on the PV cell on the other hand declines gradually with larger angles.

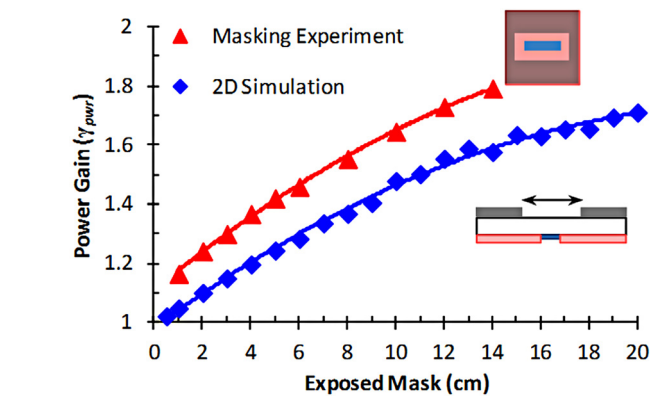
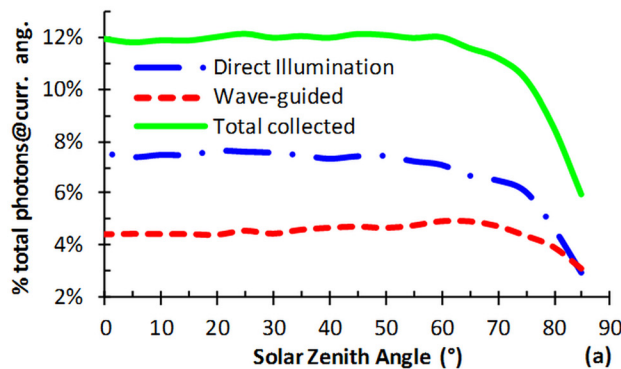


FIG. 10. Power gain versus the size of exposed LSC, comparing experimental (triangle) and simulation (diamond) results.

When summed together, the percentage of photons collected by the cell remains within 10% of the maximum up to an angle of 70°. Reflections off the waveguide top increase dramatically beyond this and are manifested by the sharp decline in photons collected. Plotting the data in terms of power gain (Fig. 12) highlights the larger proportional contribution by the LSC to gain at larger zenith angles.

The front-face orientation of the PV cells allows light to escape through the edges of the waveguide. To alleviate this issue, we consider modifying the edge surface to make it reflective, keeping light trapped in the waveguide. Doing so raises γ_{pwr} by 0.2 (Fig. 12), a 14% increment, over an unmodified LSC panel. A detailed breakdown of the photon distribution (Fig. 13) on a 22 cm wide LSC panel shows all escaping photons redirected onto the PV cell without increasing reabsorption losses. Higher LR305 concentrations or luminescent particles with larger absorption-emission curve overlaps might result in a percentage of reflected photons being reabsorbed, in which case the panel size would have to be reduced.

D. LSC loss mechanisms

In examining the loss mechanism distribution of the LSC panel constructed (Figs. 13 and 14), we can attribute the bulk of it to the narrow absorption bandwidth of LR305. Over 60% of the solar spectrum lies outside the absorption bandwidth of the luminescent dye. Expanding the absorption

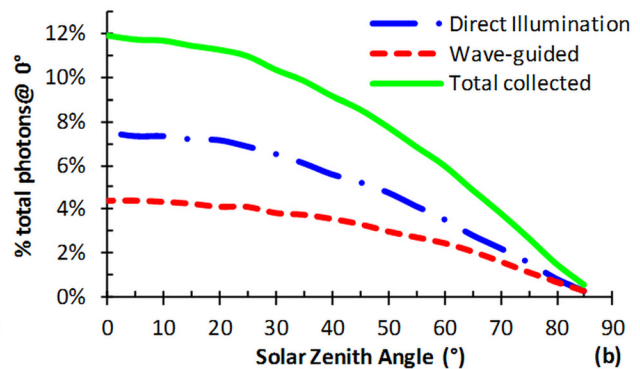


FIG. 11. Apportionment of photons collected by the PV cell as a function of the incident illumination angle. (a) % of photons referenced to the total number of incident photons on the LSC panel. Light intensity is reduced for larger angles as light is spread over a larger area; (b) % of photons referenced to the maximum number of incident photons possible (0°) on the LSC.

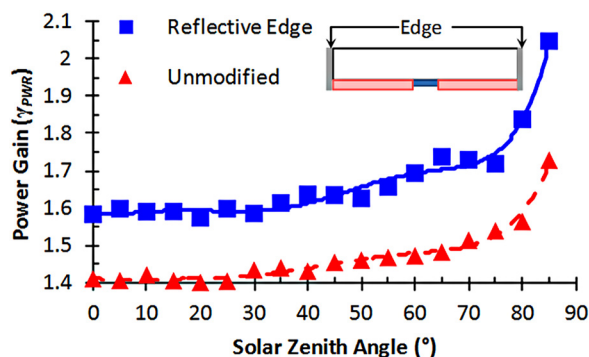


FIG. 12. Power gain as a function of the incident illumination angle, with (solid line) and without (dotted line) reflective edges.

bandwidth offers the largest potential gain, but this has to be coupled with a larger stoke shift to prevent reabsorption losses from mounting. Incident photons reflecting off the top of the waveguide give a constant 4% loss irrespective of panel size and can be suppressed with anti-reflection coatings. With the assumption that light is emitted isotropically from the luminescent dye, approximately 10% is lost from emission angles that are less than the critical angle and leave the waveguide through this escape cone. A number of solutions include increasing the refractive index of the waveguide material but the drawback is higher top reflections. Luminescent particles with anisotropic emission can be oriented to transmit light in directions favorable for total internal reflection. Reabsorption losses amount to 5% of the total photons as a result of significant overlap in the dye's emission and absorption spectrum (Fig. 4). Quantum dots with larger stoke shifts and multi-dye LSC have been proposed as viable options but care must be taken to ensure that quantum yields remain high enough to not deplete any potential gains. Reviews on LSCs, their loss mechanisms, and proposed solutions have been extensively covered in literature.^{21,43-45}

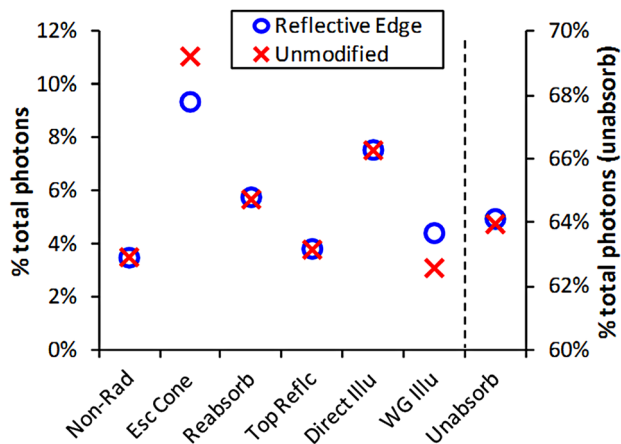


FIG. 13. Photon distribution in the LSC with (circle) and without (cross) reflective edges. Non-radiative and escape cone losses from single and multiple absorption events are classified separately. Losses from multiple absorptions are grouped collectively under re-absorption losses. Top-reflection refers to incident light reflecting off the top of the waveguide. Photons collected by the PV cell are also separated into those from direct irradiation and those channelled by the waveguide. Photons which pass through the LSC panel without undergoing any absorption or scattering are classified as unabsorbed.

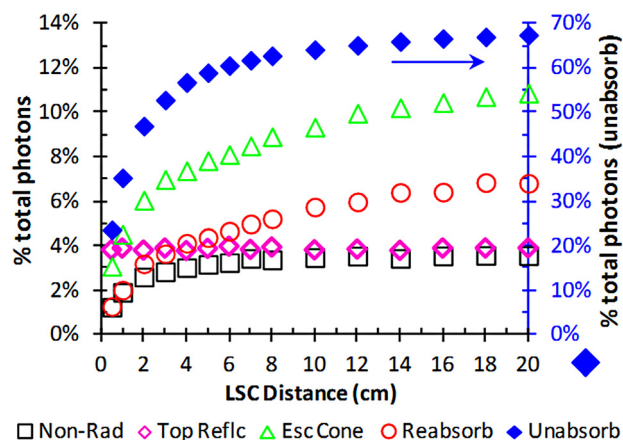


FIG. 14. Distribution of photon losses in response to increasing panel size. Similar to Fig. 13, losses from multiple absorption events are grouped into the Reabsorb category.

The sharp rise in losses from 0 to 3 cm (Fig. 14) is mostly from the drop in direct illumination following an increase in the LSC:PV-cell area. For larger panel sizes, this value becomes less significant and levels out. Non-radiative losses from first absorption events attain a constant value due to the higher quantum efficiencies provided by the LR305 dye. Losses from unabsorbed photons and escape cone will continuously increase with panel size as larger proportions of incident photons are exposed to the luminescent layer. As expected, re-absorption losses show an initial faster rise with panel size due to the increase probability of absorption with distance travelled. But as each reabsorption event can only result in emitted photons with longer wavelengths, a red-shift occurs in the emission spectrum profile until no overlap occurs with the absorption spectrum and a plateau is eventually reached.

IV. SUMMARY AND CONCLUSIONS

Results from the LSC model closely parallel the behavior of data collected from the experimental mock up panels. This enables the model to reasonably predict the dimensions and layout of a LSC panel for the desired performance parameter. By tracking the photon's path of travel and analyzing its final outcome, a greater appreciation on the physical mechanisms at work is obtained. Scrutinizing the distribution of the photon outcomes reveals the effect of various design parameters on the power gain, effective operating angles, and loss mechanisms in the LSC panel.

ACKNOWLEDGMENTS

The authors would like to thank members of Aler's Photovoltaics (APV) for sharing their knowledge on panel construction and their help in data collection. This work was supported by the UC Discovery Grant No. 192864.

¹B. S. Richards, *Sol. Energy Mater. Sol. Cells* **90**, 2329 (2006).

²L. H. Slooff, E. E. Bende, A. R. Burgers, T. Budel, M. Pravettoni, R. P. Kenny, E. D. Dunlop, and A. Büchtemann, *Phys. Status Solidi* **2**, 257 (2008).

- ³L. H. Slooff, R. Kinderman, A. R. Burgers, A. Büchtemann, R. Danz, T. B. Meyer, A. J. Chatten, D. Farrell, K. W. J. Barnham, and J. A. M. van Roosmalen, *Proc. SPIE* **6197**, 61970K (2006).
- ⁴W. G. J. H. M. van Sark, K. W. J. Barnham, L. H. Slooff, A. J. Chatten, A. Büchtemann, A. Meyer, S. J. McCormack, R. Koole, D. J. Farrell, R. Bose, E. E. Bende, A. R. Burgers, T. Budel, J. Quilitz, M. Kennedy, T. Meyer, C. D. M. Donegá, A. Meijerink, and D. Vanmaekelbergh, *Opt. Express* **16**, 21773 (2008).
- ⁵R. Koeppe, N. S. Sariciftci, and A. Büchtemann, *Appl. Phys. Lett.* **90**, 181126 (2007).
- ⁶V. Sholin, J. D. Olson, and S. A. Carter, *J. Appl. Phys.* **101**, 123114 (2007).
- ⁷M. J. Currie, J. K. Mapel, T. D. Heidel, S. Goffri, and M. A. Baldo, *Science* **321**, 226 (2008).
- ⁸G. V. Shcherbatyuk, R. H. Inman, C. Wang, R. Winston, and S. Ghosh, *Appl. Phys. Lett.* **96**, 191901 (2010).
- ⁹E. Klampaftis, D. Ross, K. R. McIntosh, and B. S. Richards, *Sol. Energy Mater. Sol. Cells* **93**, 1182 (2009).
- ¹⁰C. Strümpel, M. McCann, G. Beaucarne, V. Arkhipov, A. Slaoui, V. Švrček, C. del Cañizo, and I. Tobias, *Sol. Energy Mater. Sol. Cells* **91**, 238 (2007).
- ¹¹E. Klampaftis and B. S. Richards, *Prog. Photovoltaics* **19**, 345 (2011).
- ¹²B. Norton, P. C. Eames, T. K. Mallick, M. J. Huang, S. J. McCormack, J. D. Mondol, and Y. G. Yohanis, *Sol. Energy* **85**, 1629 (2011).
- ¹³D. Chemisana, *Renewable Sustainable Energy Rev.* **15**, 603 (2011).
- ¹⁴J. W. E. Wiegman and E. van der Kolk, *Sol. Energy Mater. Sol. Cells* **103**, 41 (2012).
- ¹⁵G. Kocher-Oberlehner, M. Bardosova, M. Pemble, and B. S. Richards, *Sol. Energy Mater. Sol. Cells* **104**, 53 (2012).
- ¹⁶B. Rezaie, E. Esmailzadeh, and I. Dincer, *Energy Build.* **43**, 56 (2011).
- ¹⁷A. M. Hermann, *Sol. Energy* **29**, 323 (1982).
- ¹⁸W. H. Weber and J. Lambe, *Appl. Opt.* **15**, 2299 (1976).
- ¹⁹A. Goetzberger and W. Greube, *Appl. Phys.* **14**, 123 (1977).
- ²⁰J. S. Batchelder, A. H. Zewail, and T. Cole, *Appl. Opt.* **18**, 3090 (1979).
- ²¹B. C. Rowan, L. R. Wilson, and B. S. Richards, *IEEE J. Sel. Top. Quantum Electron.* **14**, 1312 (2008).
- ²²R. Reisfeld, *Opt. Mater.* **16**, 1 (2001).
- ²³S. J. Gallagher, B. Norton, and P. C. Eames, *Sol. Energy* **81**, 813 (2007).
- ²⁴J. Bomm, A. Büchtemann, A. J. Chatten, R. Bose, D. J. Farrell, N. L. A. Chan, Y. Xiao, L. H. Slooff, T. Meyer, A. Meyer, W. G. J. H. M. van Sark, and R. Koole, *Sol. Energy Mater. Sol. Cells* **95**, 2087 (2011).
- ²⁵C. Corrado, S. W. Leow, M. Osborn, E. Chan, B. Balaban, and S. A. Carter, *Sol. Energy Mater. Sol. Cells* **111**, 74 (2013).
- ²⁶R. Reisfeld, M. Eyal, V. Chernyak, and R. Zusman, *Sol. Energy Mater.* **17**, 439 (1988).
- ²⁷A. Mansour, *Polym. Test.* **22**, 491 (2003).
- ²⁸M. Carrascosa, S. Unamuno, and F. Agullo-Lopez, *Appl. Opt.* **22**, 3236 (1983).
- ²⁹S. J. Gallagher, P. C. Eames, and B. Norton, *Int. J. Ambient Energy* **25**, 47 (2004).
- ³⁰A. Burgers, L. Slooff, R. Kinderman, and J. Van Roosmalen, *paper presented at the 20th European Photovoltaic Solar Energy Conference and Exhibition, Barcelona, Spain* (James & James Ltd., 2005), p. 10.
- ³¹A. Schüler, A. Kostro, C. Galande, M. Valle del Olmo, E. Chambrier, and B. Huriot, in *Proceedings of ISES World Congress 2007*, edited by D. Y. Goswami and Y. Zhao (Springer, Berlin, 2009), Vols. I–V, pp. 1033–1037.
- ³²D. Şahin, B. Ilan, and D. F. Kelley, *J. Appl. Phys.* **110**, 033108 (2011).
- ³³M. Bendig, J. Hanika, H. Dammert, J. C. Goldschmidt, M. Peters, and M. Weber, in *IEEE Symposium on Interactive Ray Tracing, 2008 (RT 2008)* (IEEE, Los Angeles, CA, USA, 2008), pp. 93–98.
- ³⁴M. Kennedy, A. Chatten, D. Farrell, R. Bose, A. Büchtemann, S. McCormack, J. Doran, B. Norton, and K. Barnham, in *23rd European Photovoltaic Solar Energy Conference and Exhibition, Valencia, Spain* (2008), pp. 334–337.
- ³⁵A. J. Chatten, D. Farrel, C. Jermyn, P. Thomas, B. F. Buxton, A. Büchtemann, R. Danz, and K. W. Barnham, in *Conference Record of the Thirty-First IEEE Photovoltaic Specialists Conference, 2005* (IEEE, 2005), pp. 82–85.
- ³⁶P. Poli, L. Rota, and C. Jacoboni, *Appl. Phys. Lett.* **55**, 1026 (1989).
- ³⁷S. Portolan, R. C. Iotti, and F. Rossi, *Semicond. Sci. Technol.* **19**, S107 (2004).
- ³⁸M. Avellaneda, R. Buff, C. Friedman, N. Grandechamp, L. Kruk, and J. Newman, *Int. J. Theor. Appl. Finance* **04**, 91 (2001).
- ³⁹M. E. Mortenson, in *Computer Graphics Handbook: Geometry and Mathematics*, 1st ed. (Industrial Press, New York, NY, 1990), pp. 195–204.
- ⁴⁰J. O'Rourke, in *Computational Geometry in C*, 2nd ed. (Cambridge University Press, Cambridge, UK, 1998), pp. 220–293.
- ⁴¹S. N. Kasarova, N. G. Sultanova, C. D. Ivanov, and I. D. Nikolov, *Opt. Mater.* **29**, 1481 (2007).
- ⁴²NOAA, *NOAA Solar Calculator* (US Department of Commerce, n.d.).
- ⁴³M. G. Debije and P. P. C. Verbunt, *Adv. Energy Mater.* **2**, 12 (2012).
- ⁴⁴M. G. Debije, P. P. C. Verbunt, B. C. Rowan, B. S. Richards, and T. L. Hoeks, *Appl. Opt.* **47**, 6763 (2008).
- ⁴⁵W. R. L. Thomas, J. M. Drake, and M. L. Lesiecki, *Appl. Opt.* **22**, 3440 (1983).